Suzaku Detection of Diffuse Hard X-Ray Emission outside Vela X

Satoru Katsuda[1], Koji Mori[2], Robert Petre[1], Hiroya Yamaguchi[3], Hiroshi Tsunemi[4], Fabrizio Bocchino[5], Aya Bamba[6,7], Marco Miceli[8,5], John W. Hewitt[1], Tea Temim[1], Hiroyuki Uchida[4], and Rie Yoshii[3]

Satoru.Katsuda@nasa.gov

[1]*Code 662, NASA Goddard Space Flight Center, Greenbelt, MD 20771, U.S.A.*

[2]*Department of Applied Physics, Faculty of Engineering, University of Miyazaki, 889-2192, Japan*

[3]*RIKEN (The Institute of Physical and Chemical Research), 2-1 Hirosawa, Wako, Saitama 351-0198*

[4]*Department of Earth and Space Science, Graduate School of Science, Osaka University, 1-1 Machikaneyama, Toyonaka, Osaka 560-0043, Japan*

[5]*INAF − Osservatorio Astronomico di Palermo, Piazza del Parlamento 1, 90134 Palermo, Italy*

[6]*School of Cosmic Physics, Dublin Institute for Advanced Studies, 31 Fitzwilliam Place, Dublin 2, Republic of Ireland*

[7]*ISAS/JAXA Department of High Energy Astrophysics, 3-1-1 Yoshinodai, Chuo-ku, Sagamihara, Kanagawa 252-5210, Japan*

[8]*Dipartimento di Scienze Fisiche ed Astronomiche, Sezione di Astronomia, Universit di Palermo, Piazza del Parlamento 1, 90134 Palermo, Italy*

Abstract

Vela X is a large, $3° \times 2°$, radio-emitting pulsar wind nebula (PWN) powered by the Vela pulsar in the Vela supernova remnant. Using four Suzaku/XIS observations pointed just outside Vela X, we find hard X-ray emission extending throughout the fields of view. The hard X-ray spectra are well represented by a power-law. The photon index is measured to be constant at $\Gamma \sim 2.4$, similar to that of the southern outer part of Vela X. The power-law flux decreases with increasing distance from the pulsar. These properties lead us to propose that the hard X-ray emission is associated with the Vela PWN. The larger X-ray extension found in this work strongly suggests that distinct populations relativistic electrons form the X-ray PWN and Vela X, as was recently inferred from multiwavelength spectral modeling of Vela X.

Key words: ISM: individual (Vela Pulsar Wind Nebula) − ISM: supernova remnants − X-rays: ISM

1. Introduction

It has been universally accepted that a considerable fraction of a pulsar's spin-down energy is converted into an outflow of relativistic particles. This outflow is terminated by a strong shock resulting when the relativistic particles interact with ejecta from the host supernova remnant (SNR). High-energy particles further accelerated at this shock and diffusing downstream emit radio to TeV γ-rays via synchrotron or inverse Compton processes. The non-thermal emission is observed as a pulsar wind nebula (PWN).

One key event occurring during the evolution of a PWN (Gaensler & Slane 2006 and references therein) is its interaction with the reverse shock propagating back into the SNR interior. It is assumed that this interaction causes magnetic-field amplification and hence rapid synchrotron cooling of the highest energy (TeV) relativistic electrons. Since the cooling time of GeV electrons responsible for the radio emission is considerably longer (the lifetime of relativistic electrons inversely depends on their energy), a radio relic PWN is left behind for a long time after this interaction.

Of the more than 50 known PWNe (e.g., Kargaltsev & Pavlov 2008), the Vela PWN, associated with the middle-aged (11000 yr: Reichley et al. 1970) Vela SNR (see, figure 1), is located the nearest to Earth ($\sim$290 pc: Dodson et al. 2003). This proximity makes it an ideal target for detailed spatial studies. With its superior (sub-arcsecond) spatial resolution, Chandra X-ray Observatory revealed spectacular small-scale ($\sim$10″) structures within the Vela PWN, including jets and arcs around the pulsar (Helfand et al. 2001; Pavlov et al. 2001). These features are surrounded by a bright compact nebula emitting non-thermal X-rays, a "kidney-bean" nebula of size $\sim$2′ (Harnden et al. 1985). The spectra of these features are characterized by a power-law component, with photon index varying from $\Gamma \sim 1$ for the inner jets and arcs to $\Gamma \sim 1.5$ for the surroundings (e.g., Kargaltsev & Pavlov 2008). This system is further embedded in a large region emitting non-thermal X-rays whose power-law index ($\Gamma \sim 2$) is steeper than those in the inner regions (Markwardt & Ögelman 1995; 1998; Mangano et al. 2005; LaMassa et al. 2008). However, the full morphology of this non-thermal X-ray–emitting region (X-ray PWN) is not yet known, because Vela has not been mapped by a sufficiently broad band imaging spectrometer.

It is important for the study of the evolution of the Vela PWN and PWNe in general to map and understand the large-scale ($\sim$1°) structure of the Vela PWN across the electromagnetic spectrum. In the radio band, the Vela PWN is a network of bright filaments encompassing a large, $3° \times 2°$, region around the pulsar as shown in figure 1 (c). It is referred to as Vela X (Frail et al. 1997; Bock et al. 1998 and references therein). Vela X is asymmetric relative to the pulsar. Both the chaotic filamentation and the asymmetry led Blondin et al. (2001) to propose that Vela X arose from interaction between the PWN and the reverse shock of the Vela SNR in an inhomogeneous ambient medium. Thus, the Vela PWN is regarded as a prototype radio relic

2

PWN (Gaensler & Slane 2006). Recently, observations using HESS, AGILE, and Fermi have revealed TeV (figure 1 (d)) and GeV γ-ray (figure 1 (e)) maps (Aharonian et al. 2006; Pellizzoni et al. 2010; Abdo et al. 2010). The TeV/GeV morphologies are also asymmetric relative to the pulsar, whereas they are quite different with each other, showing chaotic structures of the Vela PWN. X-ray mapping of the Vela PWN is now ongoing. An important point is that the lifetime of relativistic electrons emitting X-rays is the shortest, because they are the most energetic (assuming the GeV and TeV emission is inverse Compton radiation). Therefore, the X-ray morphology might be different from Vela X, if Vela X is really a long-lived radio relic.

We here report on the detection of X-ray synchrotron emission beyond the boundary of Vela X, based on Suzaku/XIS data with unprecedented high sensitivity in the hard X-ray energy band (2–10 keV). Our analysis indicates that this emission is associated with the Vela PWN, strongly suggesting that the morphology of Vela PWN in X-rays is different from that in the radio (i.e., Vela X). We suggest that the X-ray PWN and Vela X are formed by distinct populations relativistic electrons, consistent with the picture inferred from recent multiwavelength spectral modeling of Vela X (LaMassa et al. 2008; de Jager et al. 2008). This implies that Vela X is indeed a radio relic of the interaction between the Vela PWN and the reverse shock.

2. Observations and Data Screening

We observed part of the Vela SNR with *Suzaku* (Mitsuda et al. 2007) in four pointings during 2010 May 2–3. We here concentrate on the data taken by the X-ray Imaging Spectrometer (XIS: Koyama et al. 2007). The XIS consists of two front-illuminated (FI: XIS0 and XIS3) CCD cameras and one back-illuminated (BI: XIS1) CCD camera. Each camera covers an identical imaging area of $17.'8 \times 17.'8$. Figure 1 (a) shows the four XIS fields of view (FOV) as white boxes labeled from P1 to P4 on a Vela SNR image from the ROSAT All-Sky Survey (RASS). Another box labeled BG shown in the figure represents the XIS FOV where we estimate local X-ray background for our spectral analysis. Figure 1 (b) shows a hard-band RASS image covering the same area in figure 1 (a), from which the Galactic SNRs Puppis A and Vela Jr. superposed along the line of sight appear as bright extended regions at the north-western (NW) and southeastern (SE) corners of the remnant, respectively, whereas the Vela PWN is not apparent. Figure 1 (c) presents a radio (843 MHz) image of the central region of the Vela SNR. The network of filaments which forms Vela X is clearly seen in the figure. Our XIS FOV are located just outside Vela X to the northeast (NE).

Using the latest CALDB files (e.g., a CTI calibration file of version 20091202), we reprocessed and cleaned the data according to the standard criteria[1] recommended by the

---

[1] See the Suzaku Data Reduction Manual which can be found from http://heasarc.gsfc.nasa.gov/docs/suzaku/analysis/abc.

calibration team of Suzaku/XIS. After the screening, the remaining exposure times are 25.3 ks, 23.2 ks, 16.8 ks, and 16.8 ks for P1, P2, P3, and P4, respectively.

3. Analysis and Results

Mosaics of the XIS images are shown in figure 2. The left and right panels show the soft (0.25–1.5 keV) and hard (1.5–5.5 keV) X-ray band images, respectively, with vignetting-corrections subtraction of the non X-ray background (NXB) caused by charged particles and γ-rays hitting the detectors (Tawa et al. 2008). Two corners of each FOV, where the calibration source of ^{55}Fe is illuminated, are masked in these images. We see strong contrasts in the soft band image (left panel). As we discuss below, this contrast is most likely caused by inhomogeneities of thermal emission from the Vela SNR. Figure 2 right shows hard X-ray emission extending throughout the FOV. This emission is at least a factor of 2 above the local background level.

As the first step of our spectral analysis, we subtract the NXB (generated by the nxbgen software: Tawa et al. 2008) from the source spectra. Figure 3 shows the NXB-subtracted XIS1 spectra (in black) extracted from the entire FOV for each observation. Then, the X-ray background is obtained from the local background region indicated in figure 1. The NXB-subtracted local-background XIS1 spectra are plotted as gray crosses in figure 3. For these, we take into account the degradation of quantum efficiency due to the build-up of contaminants on the optical blocking filter of the XIS. A detailed description of this correction can be found in the literature (e.g., Yamaguchi & Katsuda 2009). Figure 3 reveals the presence of featureless continuum emission above the background level in the hard energy band (>1.5 keV), whereas the spectra below ∼1.5 keV are dominated by line emission such as O Heα at ∼0.57 keV, O Lyα at ∼0.65 keV, and Ne Heα at ∼0.91 keV. In figure 3 bottom, we plot Suzaku spectra of Vela shrapnel B and C, and a region outside the southwestern (SW) edge of Vela Jr. (see, figure 1) along with the local background corrected for effective area. We see that these spectra do not show hard X-ray emission, indicating that (1) the hard X-ray emission in our FOV (P1–P4) does not extend to these regions and (2) the local cosmic X-ray background is quite uniform around the Vela SNR.

In the following fitting procedure, we use photons in the energy range of 0.4–11.0 keV, and employ the XSPEC software (version 12.6.0q). Since the two FI chips (XIS0 and XIS3) have similar spectral responses, their spectra are summed to improve the photon statistics. We fit the FI and BI spectra simultaneously. We manually adjust the energy scale to obtain better fits, by allowing energy-scale offsets to vary freely for the FI and the BI detectors, respectively. Before fitting, each spectrum is grouped into bins with at least ∼20 counts after subtracting the local background, which allows us to perform a χ^2 test.

We follow previous ROSAT studies, using a two-temperature collisional ionization equilibrium (CIE) plasma model (Bocchino et al. 1997; 1999; Lu & Aschenbach 2000; Miceli et al.

4

2005). It should be noted, however, that the ROSAT data have inadequate spectral resolution to reveal non-equilibrium ionization (NEI), but that NEI conditions cannot be rejected by the data (Bocchino et al. 1999; Miceli et al. 2005). In fact, recent X-ray CCD observations of several locations in the Vela SNR have revealed NEI conditions (e.g., Tsunemi et al. 1999; Katsuda & Tsunemi 2005; Yamaguchi & Katsuda 2009). We therefore employ a two-component thermal plasma model that combines NEI and CIE conditions: the hotter component (hereafter, T1) uses an NEI model, whereas the cooler component (hereafter, T2) is assumed to be in CIE, because the data cannot distinguish for it between NEI and CIE. We adopt the tbabs model (Wilms et al. 2000) for the absorption, either vnei or vpshock model (Borkowski et al. 2001) with variable abundances for T1, and the apec model (Smith et al. 2001) with solar abundances for T2, respectively. The vnei model has a single ionization timescale ($\tau = n_e t$, where n_e is the electron density and t is the time after the shock heating), whereas the vpshock model assumes a range of τ, which we take 0 to the fitted maximum value. In these thermal emission models, the solar abundances are based on Anders & Grevesse (1989). When applying this model for each spectrum from the four fields (P1–P4), we obtain the best-fit models shown in Figure 4. We find that the models are rejected with high confidence (reduced χ^2 of $\sim$2). We also find unusually high electron temperatures of a few keV and very low metal abundances below 0.1 solar values for the high-temperature component.

Addition of a power-law component resolves the uncomfortable physical conditions and results in acceptable fits (formally speaking, acceptable only if we consider systematic uncertainties). The addition of a thermal component with an electron temperature of a few keV, instead of the power-law component, also yields satisfactory fits. However, again, such a high-temperature component is not expected for evolved SNRs like Vela (11000 yr). Furthermore, the thermal component shows implausible metal abundances of $\sim$0.01 solar values. Therefore, the thermal interpretation is unlikely to be correct, and we therefore accept the non-thermal power-law interpretation. Table 1 summarizes the fit details. Figure 4 shows the XIS spectra along with the best-fit models of tbabs×(vnei + apec + power-law) and tbabs×(vpshock + apec + power-law). We find that the results from vnei and vpshock (for T1) are consistent with each other.

Possible sources for the power-law component would be either the extended Vela PWN, relativistic particles accelerated in the Vela SNR's shell, or unrelated background possibly connected to Vela Jr. The large distance between Vela Jr. and our XIS FOV (see, figure 1 (b)) make it difficult for emission from Vela Jr. to be present in our FOV. In addition, as can be found in table 1, the relatively flat photon index of $\Gamma \sim 2.4$ may rule out an association with the shell of Vela Jr. which shows a steeper photon index of $\Gamma \sim 2.8$ (e.g., Hiraga et al. 2009), though a population of relativistic particles escaping from Vela Jr. would have a flatter spectrum as lower-energy particles would be unable to diffuse as far ahead. It is also unlikely that the evolved Vela SNR show such a flat photon index, if non-thermal emission is present.

5

Although we cannot fully exclude the possibility that the hard X-ray emission is another PWN along the line of sight, the most plausible interpretation seems to be an association with the Vela PWN. We will further discuss this interpretation in the next section.

The power-law flux gradually increases from P1 to P4 by a factor of $\sim$2. The photon index is almost constant at $\Gamma \sim$2.4. One may worry about possible coupling between the photon index and other parameters. To this end, we investigate confidence contours of the photon index against the electron temperature in T1 (using vnei), the emission measure in T1 (using vnei), and the normalization in the power-law component. Figure 6 shows the confidence contours. We find conservative 90% confidence ranges of the photon index in the four FOV to be 2.2–2.6. Metal abundances are generally sub-solar and their relative abundances are consistent with the solar ratios within a factor of 2. The inferred electron temperatures ($\sim$0.1 keV and $\sim$0.3 keV) are similar to those found in the pure ISM components in the northern shell regions (Miceli et al. 2005; 2008). These results suggest that the thermal emission in our FOV is not dominated by SN ejecta but by shock-heated interstellar medium. The emission measure of T2 varies significantly from field to field, suggesting interstellar medium inhomogeneities. It should be, however, noted that absolute (relative to H) abundances are difficult to measure, especially when thermal X-ray continuum is contaminated by nonthermal continuum emission. In this context, the ejecta origin for the thermal components cannot be fully excluded. In fact, some other regions in the remnant show evidence of ejecta; e.g., the closest ejecta-dominated region to our FOV is the so-called "cocoon" located south of the pulsar (LaMassa et al. 2008; Mori et al. in preparation). Revealing the ejecta distribution in this remnant is a topic for future work.

We here examine the srcut model (Reynolds 1998) instead of the power-law model for P4. In this fitting, we fix the radio photon index to α=0.4, which is a typical value for Vela X (Alvarez et al. 2001). The radio intensity at 1 GHz is treated as either a fixed parameter or a free parameter. For the former (fixed) case, we use the intensity of 10 Jy, which is inferred from the MOST image in figure 1 (whose image resolution is 43″: Bock et al. 1998) smoothed with Suzaku's spatial resolution of 2′ (Serlemitsos et al. 2007). We allow the roll-off frequency to vary freely. The other parameters are treated as in table 1. We find that the srcut model does not fit as well as the power-law model (χ^2 values are 879 or 519 for fixed or free radio intensity, respectively). Nonetheless, we note that the best-fit radio intensity inferred from the srcut model of the latter case is $\sim$0.01 Jy, which is three orders of magnitude smaller than that of Vela X. This might imply that X-ray emission is not associated with Vela X.

4. Discussion

Utilizing the high sensitivity of the XIS, we found diffuse, hard X-ray emission in four FOV located $\sim$0.°6–1.°6 northeast of the Vela pulsar. They are thus located just outside Vela X, a network of radio filaments that has been suggested to be a relic of interaction between the PWN and the reverse shock. The hard X-ray spectra are featureless and are well represented

by a power-law component. Figure 7 shows photon index (circles) and flux (triangles) of the power-law component as a function of the distance from the Vela pulsar, which is derived using the vnei model for the T1 component (see, table 1). We see that the photon index is almost constant at $\Gamma \sim 2.4$, consistent with that found in the southern outer region of Vela X (LaMassa et al. 2008; Mori et al. in preparation). On the other hand, the power-law flux gradually decreases with increasing distance from the pulsar. Moreover, the power-law component becomes negligible at larger distances from the pulsar, including regions in the northern shell (Miceli et al. 2005; 2006; 2008) and the Vela shrapnel to the east (Tsunemi et al. 1999; Miyata et al. 2001; Katsuda & Tsunemi 2005; 2006; Yamaguchi & Katsuda 2009). These facts suggest that the hard X-ray emission found in our FOV is related to the Vela PWN, and thus the PWN in X-ray extends beyond the radio PWN (i.e., Vela X). We note that other evolved PWNe associated with PSR J1826–1334 (Uchiyama et al. 2009) and PSR J1809–193 (Anada et al. 2010) share the large-scale (> several pc) photon index uniformity, in contrast to young PWNe where the spectrum hardens toward the pulsars (e.g., Mori et al. 2004 and references therein).

Our finding that the X-ray Vela PWN extends farther than Vela X provides us with important insight into the origin of relativistic electrons. The mechanisms that potentially limit PWN size are synchrotron cooling, diffusion, or convection (advection) of the relativistic electrons. If cooling is important and relativistic electrons systematically flow outward, the X-ray size must be smaller than the radio size, since the lifetime of X-ray–emitting high-energy (TeV) electrons is much shorter than that of radio-emitting low-energy (GeV) electrons. An example for such PWNe would be the Crab nebula. In the other cases, the size would be independent of wavelength; in other words, the size in X-ray and radio would be identical like 3C 58. Our result, X-ray–emitting particles beyond the radio-emitting particles, is inconsistent with these expectations. This difficulty can be resolved, however, if we postulate that the X-ray–emitting electrons are not physically related to those forming Vela X. In fact, recent multiwavelength spectral modeling of the non-thermal emission in the cocoon have suggested an excess of low-energy (GeV) electrons (LaMassa et al. 2008; de Jager et al. 2008; Pellizzoni et al. 2010; Abdo et al. 2010). Thus, our result provides strong support for the idea that distinct populations relativistic electrons generate the X-ray PWN and Vela X from an independent, morphological point of view.

We here speculate how the X-ray PWN becomes more extended than the radio PWN (Vela X). Numerical simulations show that the reverse shock formed in the SNR starts crushing the PWN on a time scale of $\sim$3000 yr after the SN explosion (Blondin et al. 2001; Bucciantini et al. 2003). During the next $\sim$3000 yr or so, hydrodynamic instabilities at the contact discontinuity between the SN ejecta and the PWN create filamentary features, which probably have amplified magnetic fields, which in turn radiate synchrotron emission efficiently. This is the process considered to be the origin of Vela X. Given an SNR age of 11000 yr, the age of Vela X would therefore be roughly 5000 yr. Because the lifetime of radio-emitting electrons is longer

than the age of the Vela SNR, it is possible that these filamentary features have persisted as Vela X since its birth (Blondin et al. 2001). On the other hand, the lifetime of the relativistic electrons emitting synchrotron X-rays is much shorter. Using the most recent estimate of the magnetic field B=4 μG in the cocoon (and halo) of Vela X (Abdo et al. 2010), the synchrotron cooling time for electrons emitting synchrotron X-rays with a characteristic energy E_{syn}=2 keV is ~3400 (B/4 μG)$^{-1.5}$(E_{syn}/2 keV)$^{-0.5}$ yr (de Jager & Djannati-Ataï 2008). This lifetime is less than the estimated age of Vela X. Further, if we consider that magnetic fields were amplified at the time of interaction between the reverse shock and the PWN, then the lifetime is even shorter. Therefore, most electrons, which had emitted synchrotron X-rays when Vela X was created, have already burned-out. In this case, it is reasonable to consider that the source of X-ray emission in the Vela PWN is a fresh population of high-energy electrons that overran the radio relic (Vela X). Whereas this interpretation seems likely, we should keep in mind that the estimates of the age of Vela X (~5000 yr) and the lifetime of X-ray–emitting relativistic electrons (~3400 yr) are quite uncertain; both estimates are not as accurate as ~50%. Therefore, at this point we cannot rule out other more exotic possibilities, e.g., somewhat lower-energy electrons at the edge of Vela X are now encountering higher magnetic fields for some reason, in which they can radiate X-rays.

Based on systematic studies of PWNe using Suzaku and Chandra, Bamba et al. (2010) report that X-ray PWNe continue to expand until an age of ~100 kyr. Figure 3 in Bamba et al. (2010), showing X-ray size vs. characteristic age for 8 PWNe, suggests that the X-ray size of the Vela PWN at an age of 11000 yr should be ~5–10 pc. The farthest edge of our XIS FOV is ~8 pc away from the pulsar (at a distance of 290 pc), within the size range inferred for other PWNe. To investigate how the X-ray PWN expands to such an extent is left for future work. To do this, we need more information on the extent and morphology of the hard X-rays.

So far, the only large-scale (~ 1°) map of the X-ray synchrotron nebula around the Vela pulsar is the significance-contour map in 2.5–10 keV range by Willmore et al. (1992) who used the Birmingham coded mask telescope. The authors found a diffuse, hard X-ray feature extending approximately 1° to the NE and SW, and interpreted it to originate from the Vela PWN. Its NE edge corresponds to our innermost (the nearest to the pulsar) XIS FOV, P4, where we find the strongest intensity of hard X-ray emission among the four (P1–P4) FOV. Therefore, it appears that the Suzaku/XIS has unveiled that the PWN extends beyond the NE edge defined by Willmore et al. (1992). However, we suspect that the significance-contour map does not reflect a true hard X-ray map. For example, the map does not show Vela Jr. whose NW rim is more than 10 times brighter than P4 and thus should have been detected (1–5 keV: Pannuti et al. 2010). Moreover, it should be noted that the significance level of the suggested PWN feature is not very high, only 1.5–3 sigma. In fact, there are a number of such low-significance hot spots in the map. Most of these features do not have counterparts in other wavelengths. While the authors interpreted that they are blobs of material

8

at a wide range of temperatures, an alternative interpretation would be that they are just statistical noise. Given these considerations, we believe that the map presented in Willmore et al. (1992) is not conclusive. Dedicated observations of Vela X and its surroundings with X-ray CCD spectrometers such as Suzaku/XIS or XMM-Newton/EPIC are eagerly desired to reveal definitive structures of the X-ray Vela PWN as well as to investigate the evolution of PWNe in general.

5. Conclusion

We have detected hard X-ray emission just outside Vela X, using four Suzaku/XIS observations. Our analysis suggests that it is of power-law origin and is associated with Vela PWN. However, the fact that the X-ray extent is larger than Vela X strongly suggests that the hard X-ray emission is not related to Vela X, invoking distinct populations relativistic electrons for the X-ray PWN and Vela X—an interpretation recently inferred from multiwavelength spectral modelings of Vela X (LaMassa et al. 2008; de Jager et al. 2008). Our finding of the large extent of the X-ray PWN would require further observations to unveil structures of the Vela PWN.

References

Abdo, A. A., et al. 2010, ApJ, 713, 146

Alvarez, H., Aparici, J., May, J., & Reich, P. 2001, A&A, 372, 636

Anada, T., Bamba, A., Ebisawa, K., & Dotani, T. 2010, PASJ, 62, 179

Anders, E., & Grevesse, N. 1989, Geochim. Cosmochim. Acta, 53, 197

Aharonian, F., et al. 2006, A&A, 448, L43

Bamba, A., Anada, T., Dotani, T., Mori, K., Yamazaki, R., Ebisawa, K., & Vink, J. 2010, ApJ, 719, L116

Blondin, J. M., Chevalier, R. A., & Frierson, D. M. 2001, ApJ, 563, 806

Bocchino, F., Maggio, A., & Sciortino, S. 1997, A&A, 481, 872

Bocchino, F., Maggio, A., & Sciortino, S. 1999, A&A, 342, 839

Bock, D. C.-J., Turtle, A. J., & Green, A. J. 1998, AJ, 116, 1886

Borkowski, K. J., Lyerly, W. J., & Reynolds, S. P. 2001, ApJ, 548, 820

Bucciantini, N., Blondin, J. M., Del Zanna, L., & Amato, E. 2003, A&A, 405, 617

Gaensler, B. M., & Slane, P. O. 2006, A&AR, 44, 17

de Jager, O. C., Slane, P. O., & LaMassa, S. 2008, ApJ, 689, L125

de Jager, O. C., & Djannati-Ataï, A. 2008, in Lect. Notes Phys., Neutron Stars and Pulsars, ed. W. Becker (Berlin: Springer)

Dodson, R., Legge, D., Reynolds, J. E., & McCulloch, P. M. 2003, ApJ, 596, 1137

Frail, D. A., Bietenholz, M. F., Markwardt, C. B., & Ögelman, H. 1997, ApJ, 475, 224

Harnden, F. R. Jr., Grant, P. D., Seward, F. D., & Kahn, S. M. 1985, ApJ, 299, 828

Helfand, D. J., Gotthelf, E. V., & Halpern, J. P. 2001, ApJ, 556, 380

Hiraga, J. S., et al. 2009, PASJ, 61, 275

Kargaltsev, O., & Pavlov, G. G. 2008, in AIP Conf. Series, Vol. 983, 40 Years of Pulsars: Millisecond Pulsars, Magnetars and More, ed. C. Bassa, Z. Wang, A. Cumming, & V. M. Kaspi, 171–185

Katsuda, S., & Tsunemi, H. 2005, PASJ, 57, 621

Katsuda, S., & Tsunemi, H. 2006, ApJ, 642, 917

Koyama, K., et al. 2007, PASJ, 59, S23

LaMassa, S. M., Slane, P. O., & de Jager, O. C. 2008, ApJ, 689, L212

Lu, F. J., & Aschenbach, B. 2000, A&A, 362, 1083

Mangano, V., Massaro, E., Bocchino, F., Mineo, T., & Cusumano, G. 2005, A&A, 436, 917

Markwardt, C. B., & Ögelman, H. 1995, Nature, 375, 40

Markwardt, C. B., & Ögelman, H. 1997, ApJ, 480, L13

Miceli, M., Bocchino, F., Maggio, A., & Reale, F. 2005, A&A, 442, 513

Miceli, M., Reale, F., Orlando, S., & Bocchino, F. 2006, A&A, 458, 213

Miceli, M., Bocchino, F., & Reale, F. 2008, ApJ, 676, 1064

Mitsuda, K., et al. 2007, PASJ, 59, S1

Miyata, E., Tsunemi, H., Aschenbach, B., & Mori, K. 2001, ApJ, 559, L45

Mori, K., Burrows, D. N., Hester, J. J., Pavlov, G. G., Shibata, S. & Tsunemi, H. 2004, ApJ, 609, 186

Pannuti, T. G., Allen, G. E., Filipovic, M. D., de Horta, A. Stupar, M., & Agrawal, R. 2010, ApJ, 721, 1492

Pavlov, G. G., Kargaltsev, O. Y., Sanwal, D., & Garmire, G. P. 2001, ApJ, 554, L189

Pellizzoni, A., et al. 2010, Science, 327, 663

Reichley, P. E., Downs, G. S., & Morris, G. A. 1970, ApJ, 159, L35

Reynolds, S. P. 1998, ApJ, 493, 375

Serlemitsos, P. J., et al. 2007, PASJ, 59, S9

Smith, R. K., Brickhouse, N. S., Liedahl, D. A., & Raymond, J. C. 2001, ApJ, 556, L91

Tawa, N., et al. 2008, PASJ, 60, S11

Tsunemi, H., Miyata, E., & Aschenbach, B. 1999, PASJ, 51, 711

Uchiyama, H., Matsumoto, H., Tsuru, T. G., Koyama, K., & Bamba, A. 2009, PASJ, 61, S189

Yamaguchi, H., & Katsuda, S. 2009, ApJ, 696, 1548

Willmore, A. P., Eyles, C. J., Skinner, G. K., & Watt, M. P. 1992, MNRAS, 254, 139

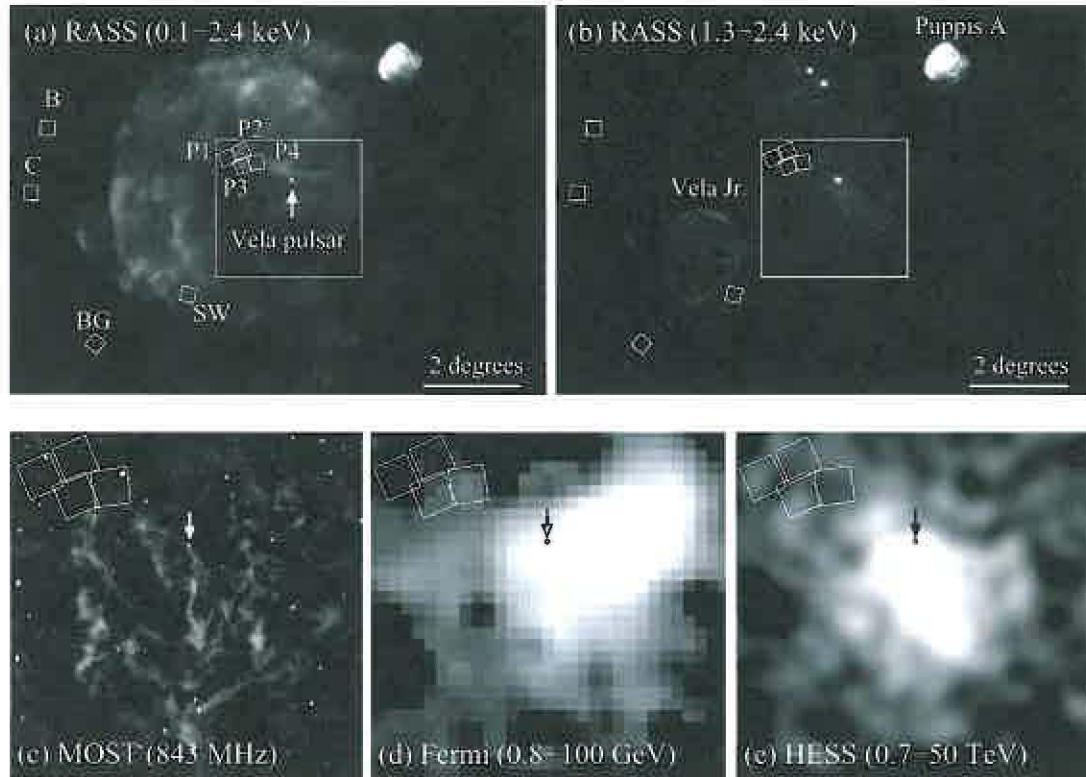Wilms, J., Allen, A., & McCray, R. 2000, ApJ, 542, 914

Fig. 1. (a) RASS X-ray (0.1–2.4 keV) image of the entire Vela SNR. The effects of vignetting and exposure are corrected. The intensity scale is square root. The Suzaku/XIS FOV ($17'.8 \times 17'.8$) are shown as white boxes labeled P1–P4 (for source regions), BG (for local background), B, C, and SW (for Vela shrapnel B and C, and outside the SW edge of Vela Jr., respectively). (b) Same as (a) but for the 1.3–2.4 keV band. Galactic SNRs Puppis A and Vela Jr. superposed along the line of sight can be seen in the NE edge or SE corner of the Vela SNR. (c) MOST radio (843 MHz) image covering Vela X region (the white boxes in figure 1 (a) and (b)), with its network of filaments (Bock et al. 1998). The intensity scale is square root. The XIS FOV are located just outside Vela X. The arrow indicates the location of the Vela pulsar. (d) Same as (c) but for Fermi (0.8–100 GeV) image, which a test statistic map as in Abdo et al. (2010). (e) Same as (c) but for HESS (0.7–50 TeV) image, which is taken from Aharonian et al. (2006).
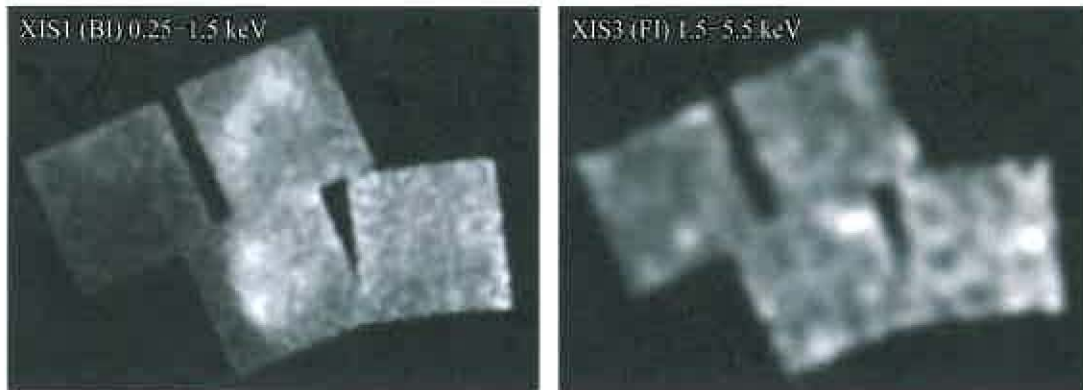
Fig. 2. Left: Linearly-scaled XIS1 image in an energy range of 0.25–1.5 keV. The effects of vignetting and exposure are corrected after subtraction of the NXB emission. The image has been smoothed with a Gaussian kernel of σ=50″. Two corners of each FOV. Right: Same as left but obtained by XIS3 in the 1.5–5.5 keV band, and smoothed with a Gaussian kernel of σ=117″.
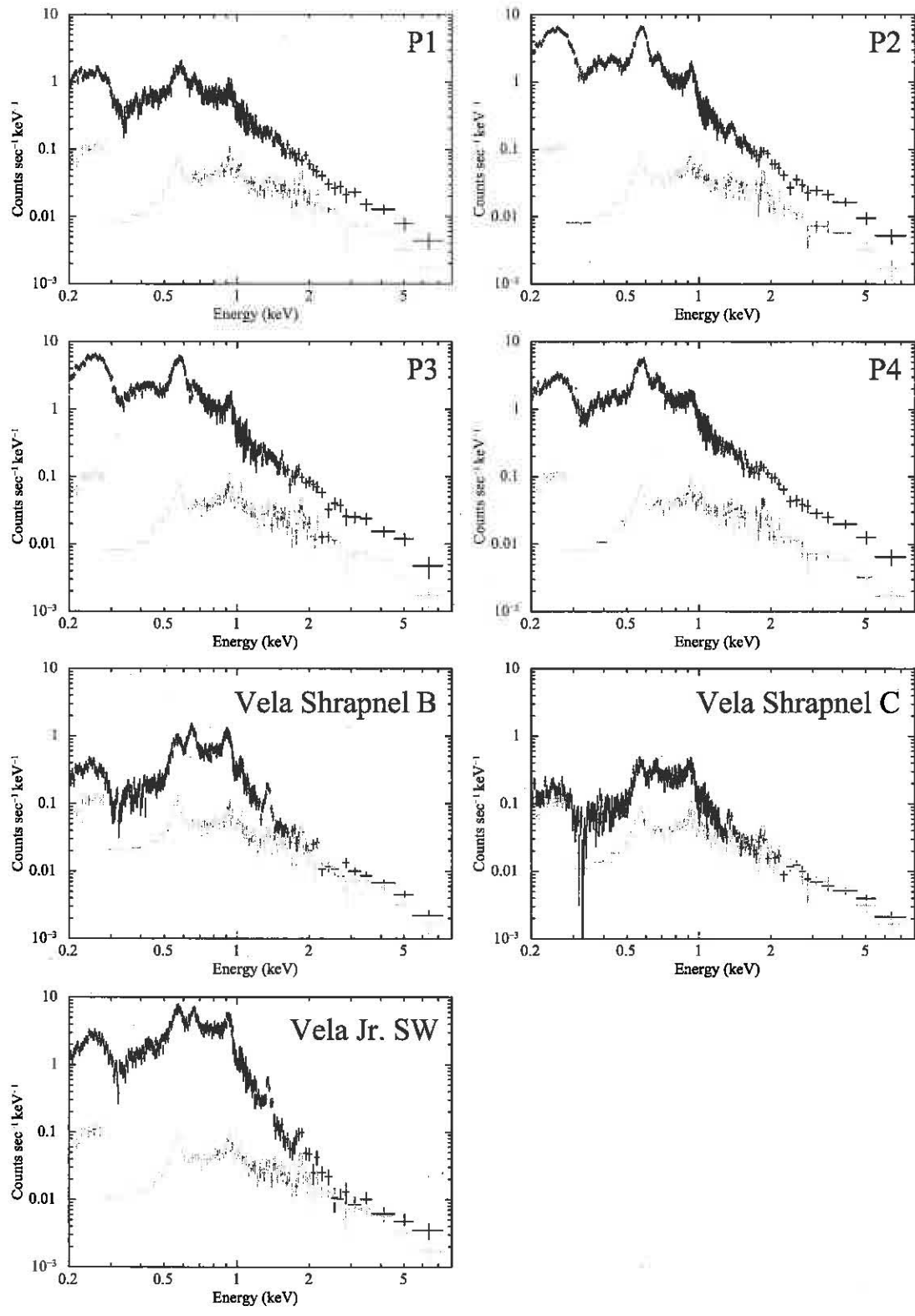
Fig. 3. NXB-subtracted source spectra (in black) and a local background (in gray). The spectra are extracted from the entire FOV. The background spectra are corrected for the degradation of quantum efficiency after NXB subtraction.
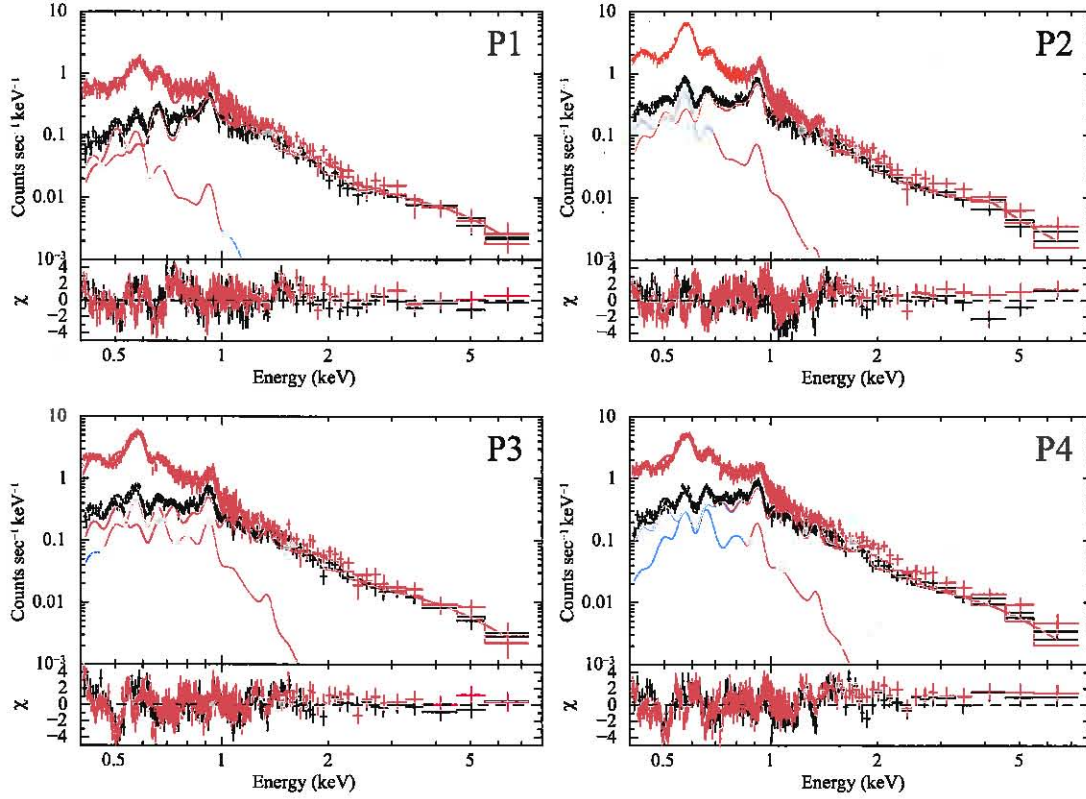
13

Fig. 4. XIS spectra along with the best-fit model consisting of two thermal components. Red and black correspond to XIS1 and XIS0+3, respectively. Contributions of each component (`apec` in light blue and `vnei` in orange) are separately illustrated only for XIS0+3. Lower panels show residuals between the data and the best-fit model.
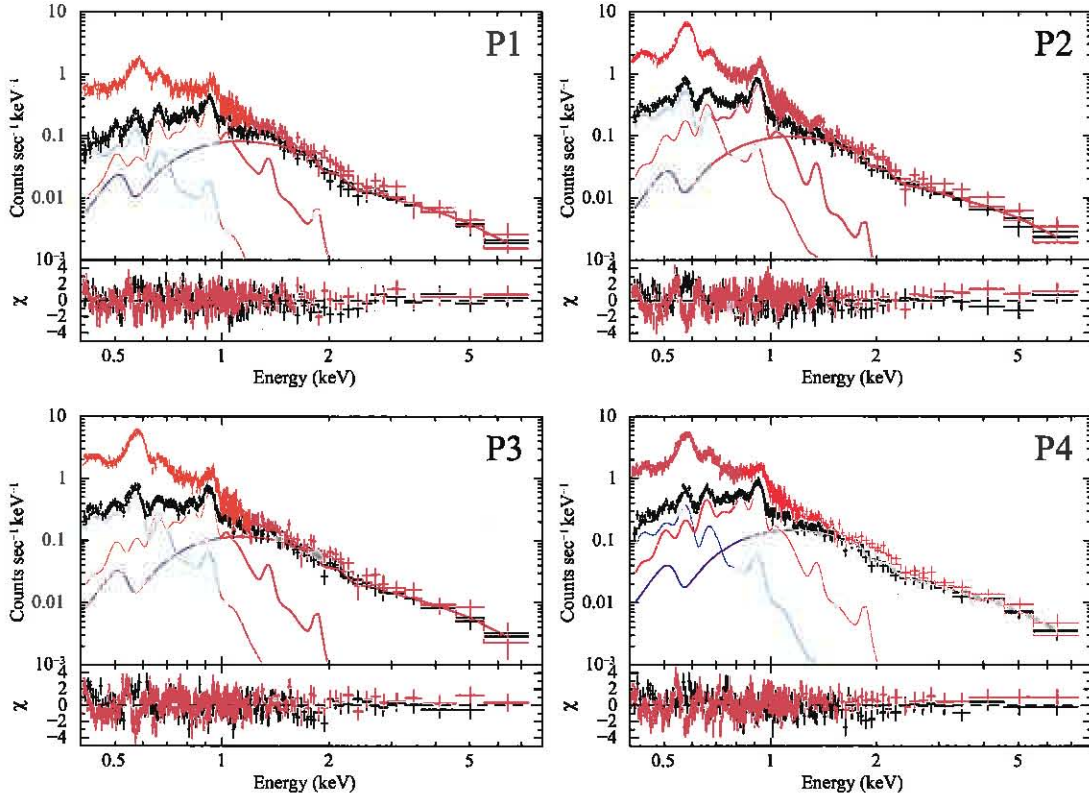
14

Fig. 5. XIS spectra along with the best-fit model. Red and black correspond to XIS1 and XIS0+3, respectively. Contributions of each component (`apec` in light blue, `vnei` in orange, and `power-law` in blue) are separately illustrated only for XIS0+3. Lower panels show residuals between the data and the best-fit model.
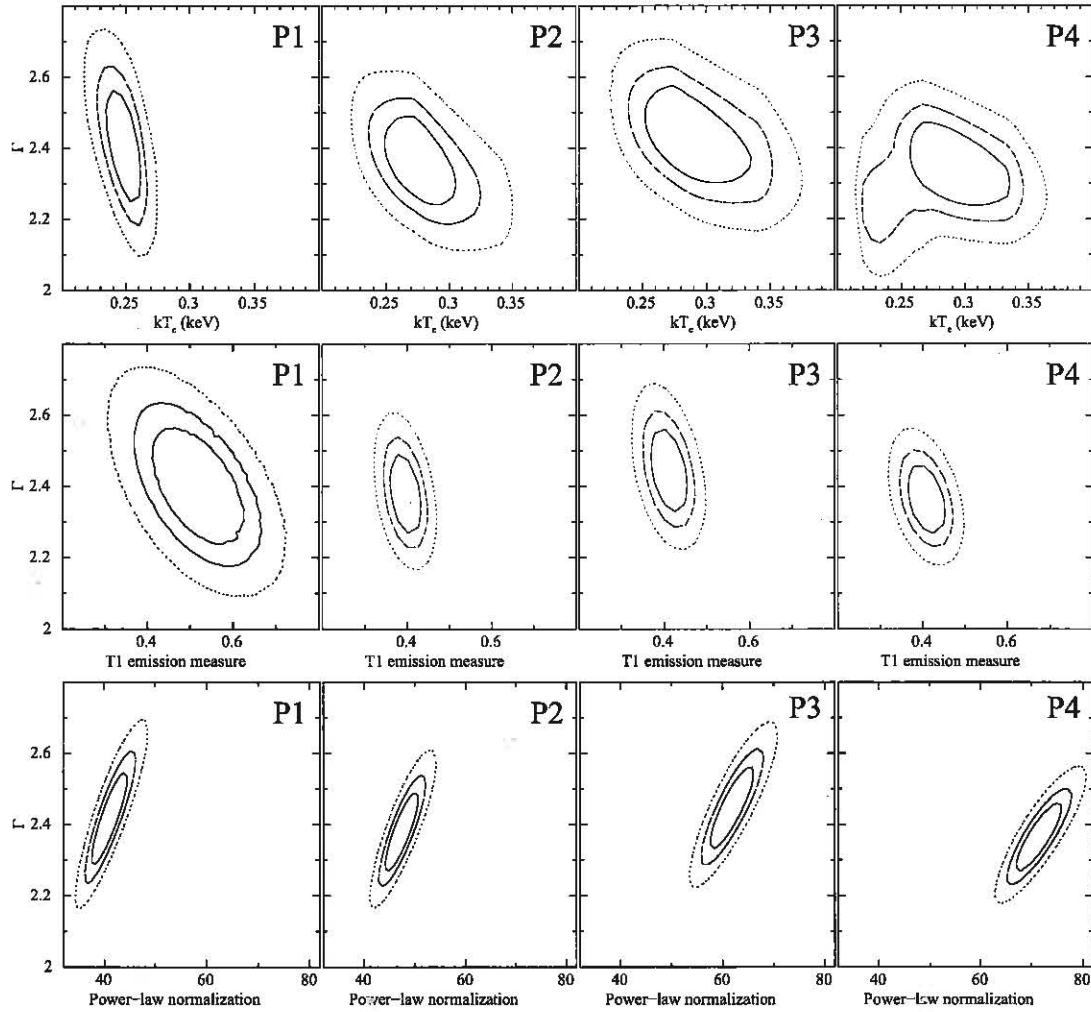
Fig. 6. Confidence contours at 68% (solid), 90% (dashed), and 99% (dotted) for Γ vs. the electron temperature in T1 (top panels), Γ vs. the emission measure in T1 (middle panels), and Γ vs. normalization in the power-law component (bottom panels). We use the vnei model for the T1 component. For the middle and bottom panels, we calculate the significance level after fixing the electron temperature and the ionization timescale in T1. Emission measures in the middle panels are in units of $10^{18} cm^{-5}$. Normalizations in the bottom panels are in unit of photons $keV^{-1} cm^{-2} s^{-1} str^{-1}$ at 1 keV.

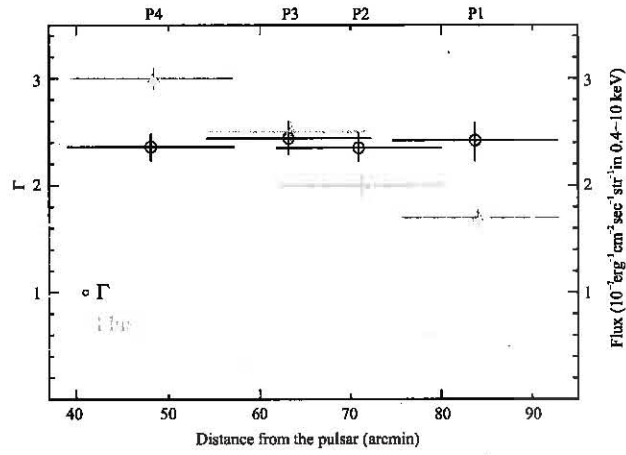**Fig. 7.** Photon indices (black circles) and fluxes (grey triangles) of the power-law component as a function of the distance from the Vela pulsar. The data points for the photon indices and fluxes are slightly displaces horizontally for clarity.

17

Table 1. Spectral-fit parameters using a two-thermal-components plus one-powerlaw-component model.[*]

Parameter	P1		P2		P3		P4	
Interstellar absorption: tbabs								
$N_{\rm H}$ ($10^{20}\,{\rm cm}^{-2}$)				3 (fixed)				
High-temperature component: vnei or vpshock								
	vnei	vpshock	vnei	vpshock	vnei	vpshock	vnei	vpshock
$kT_{\rm e}$ (keV)	$0.25^{+0.02}_{-0.01}$	$0.24^{+0.03}_{-0.01}$	$0.27^{+0.04}_{-0.02}$	0.27 ± 0.03	$0.28^{+0.06}_{-0.03}$	0.30 ± 0.05	$0.29^{+0.06}_{-0.03}$	$0.30^{+0.05}_{-0.04}$
O (solar)	$0.28^{+0.06}_{-0.06}$	$0.27^{+0.02}_{-0.02}$	$0.52^{+0.05}_{-0.03}$	$0.45^{+0.02}_{-0.05}$	$0.45^{+0.06}_{-0.06}$	$0.39^{+0.02}_{-0.03}$	$0.49^{+0.06}_{-0.05}$	$0.45^{+0.04}_{-0.05}$
Ne (solar)	0.62 ± 0.16	$0.64^{+0.12}_{-0.04}$	$1.14^{+0.15}_{-0.18}$	0.98 ± 0.11	$0.81^{+0.15}_{-0.16}$	$0.65^{+0.08}_{-0.05}$	$0.98^{+0.15}_{-0.18}$	$0.80^{+0.13}_{-0.05}$
Mg (solar)	$0.43^{+0.22}_{-0.2}$	0.45 ± 0.2	0.39 ± 0.2	$0.36^{+0.19}_{-0.17}$	$0.29^{+0.22}_{-0.21}$	$0.28^{+0.18}_{-0.16}$	0.29 ± 0.19	$0.26^{+0.16}_{-0.15}$
Fe (solar)	$0.29^{+0.06}_{-0.10}$	$0.31^{+0.04}_{-0.03}$	$0.53^{+0.09}_{-0.10}$	$0.53^{+0.04}_{-0.07}$	$0.50^{+0.11}_{-0.12}$	$0.49^{+0.11}_{-0.06}$	$0.59^{+0.11}_{-0.12}$	$0.53^{+0.05}_{-0.06}$
$\log\{\tau({\rm cm}^{-3}\,{\rm sec})\}$	>12	—	10.89 ± 0.16	—	$10.78^{+0.18}_{-0.22}$	—	$11.02^{+0.36}_{-0.25}$	—
$\tau_{\rm lower}$ (${\rm cm}^{-3}\,{\rm sec}$)	—	0 (fixed)	—	0 (fixed)	—	0 (fixed)	—	0 (fixed)
$\log\{\tau_{\rm upper}({\rm cm}^{-3}\,{\rm sec})\}$	—	>12	—	$11.26^{+0.18}_{-0.15}$	—	$11.00^{+0.09}_{-0.19}$	—	$11.25^{+0.32}_{-0.22}$
EM[†] ($10^{18}\,{\rm cm}^{-5}$)	$0.51^{+0.12}_{-0.09}$	$0.52^{+0.06}_{-0.02}$	$0.39^{+0.10}_{-0.09}$	$0.48^{+0.03}_{-0.06}$	$0.41^{+0.12}_{-0.11}$	$0.45^{+0.03}_{-0.09}$	$0.41^{+0.17}_{-0.11}$	$0.46^{+0.02}_{-0.05}$
Observed flux[‡]	2.1 ± 0.1	2.1 ± 0.1	6.8 ± 0.3	7.2 ± 0.2	7.0 ± 0.3	7.8 ± 0.2	6.5 ± 0.3	7.9 ± 0.2
Unabsorbed flux[‡]	2.7 ± 0.1	2.6 ± 0.1	8.7 ± 0.3	9 ± 0.2	7.9 ± 0.3	9.8 ± 0.3	6.8 ± 0.3	9.8 ± 0.2
Low-temperature component: apec								
$kT_{\rm e}$ (keV)	0.09 ± 0	0.09 ± 0.01	0.09 ± 0.01	0.09 ± 0.01	0.08 ± 0.01	0.08 ± 0.01	0.09 ± 0.01	0.09 ± 0.01
EM[†] ($10^{18}\,{\rm cm}^{-5}$)	1.7 ± 0.3	$1.6^{+0.4}_{-0.2}$	$7.3^{+0.8}_{-0.9}$	6.2 ± 0.6	$13.1^{+4.8}_{-5.0}$	$7.4^{+5.1}_{-1.8}$	$4.7^{+0.6}_{-0.7}$	$3.4^{+0.7}_{-0.8}$
Observed flux[‡]	2.1 ± 0.1	2.0 ± 0.1	6.6 ± 0.3	6.3 ± 0.3	5.9 ± 0.3	5.3 ± 0.2	5.2 ± 0.3	3.9 ± 0.3
Unabsorbed flux[‡]	2.7 ± 0.1	2.6 ± 0.1	8.7 ± 0.3	8.4 ± 0.3	7.9 ± 0.3	7 ± 0.3	6.8 ± 0.3	5.2 ± 0.3
Hard-tail component: power-law								
Γ	$2.42^{+0.16}_{-0.19}$	$2.34^{+0.17}_{-0.06}$	$2.35^{+0.15}_{-0.12}$	$2.33^{+0.12}_{-0.11}$	2.44 ± 0.15	$2.38^{+0.10}_{-0.17}$	$2.36^{+0.12}_{-0.13}$	$2.28^{+0.14}_{-0.08}$
Norm[§]	$41.0^{+4.8}_{-3.0}$	$38.3^{+1.8}_{-3.1}$	$46.6^{+4.3}_{-4.5}$	$45.5^{+3.1}_{-2.5}$	$61.6^{+5.5}_{-3.4}$	$57.3^{+2.7}_{-6.6}$	$71.2^{+6.2}_{-7.2}$	$67.9^{+3.6}_{-3.1}$
Observed flux[‡]	1.6 ± 0.1	1.6 ± 0.1	1.8 ± 0.1	1.8 ± 0.1	2.3 ± 0.1	2.2 ± 0.1	2.8 ± 0.1	2.7 ± 0.1
Unabsorbed flux[‡]	1.7 ± 0.1	1.7 ± 0.1	2 ± 0.1	2 ± 0.1	2.5 ± 0.1	2.4 ± 0.1	3 ± 0.1	2.9 ± 0.1
Offset (eV)	+0.9, +10.9	+0.9, +10.8	0.0, +6.9	0.0, +7.2	0.0, +6.9	+0.2, +6.0	+0.4, +8.5	+0.3, +8.0
χ^2/d.o.f.	400/387	401/387	511/387	520/387	538/387	536/387	507/387	506/387

[*] Other elements are fixed to the solar values. The values of abundances are multiples of solar values. The errors are in the range $\Delta\chi^2 < 2.7$. The fixed $N_{\rm H}$-value is determined by fitting the Vela pulsar's spectrum with a blackbody model (Mori et al. in preparation).

[†] EM denotes the emission measure $\int n_{\rm e} n_{\rm H} d\ell$, where $n_{\rm H}$ is the number density of protons and $d\ell$ is the X-ray–emitting plasma depth.

[‡] In unit of $10^{-7}\,{\rm erg\,cm}^{-2}\,{\rm sec}^{-1}\,{\rm str}^{-1}$ in a range of 0.4–10 keV.

[§] In unit of ${\rm photons\,keV}^{-1}\,{\rm cm}^{-2}\,{\rm s}^{-1}\,{\rm str}^{-1}$ at 1 keV.